Zhigang Zang
Shuangyi Zhao
Wensi Cai
Huaxin Wang

Inorganic Perovskite Materials and Devices

Springer

Springer Series in Materials Science

Volume 343

The Springer Series in Materials Science covers the complete spectrum of materials research and technology, including fundamental principles, physical properties, materials theory and design. Recognizing the increasing importance of materials science in future device technologies, the book titles in this series reflect the state-of-the-art in understanding and controlling the structure and properties of all important classes of materials.

Zhigang Zang · Shuangyi Zhao · Wensi Cai ·
Huaxin Wang

Inorganic Perovskite Materials and Devices

Zhigang Zang [ID]
College of Optoelectronic Engineering
Chongqing University
Chongqing, China

Shuangyi Zhao [ID]
College of Optoelectronic Engineering
Chongqing University
Chongqing, China

Wensi Cai [ID]
College of Optoelectronic Engineering
Chongqing University
Chongqing, China

Huaxin Wang
College of Optoelectronic Engineering
Chongqing University
Chongqing, China

If disposing of this product, please recycle the paper.

Preface

Perovskite materials, which consist of metals and halogens, have been considered as the "star material" and good candidates in next-generation optoelectronics. Among perovskite materials, owing to prominent properties, such as high emission efficiencies, strong optical absorption, long carrier diffusion lengths, accepted defect tolerance and excellent stabilities, inorganic perovskites have been employed in various optoelectronic fields, including solar cells, light-emitting diodes, electronic devices, as well as photodetectors and high-energy radiation detectors. This book introduces synthesis methods and their optoelectronic properties of inorganic perovskites, providing guidance for researchers to better understand synthesis processes, structures, properties and applications of inorganic perovskites.

In this book, components and structures of inorganic lead halide and lead-free metal halide perovskites are firstly introduced and analyzed in Chap. 1. Electronic and optical properties of inorganic perovskites with different dimensionalities and configurations are summarized in detail. Then, Chap. 2 of this book introduces reported synthesis methods of inorganic perovskite nanocrystals, thin films and single crystals, in which features of mentioned methods have been described. Furthermore, advances of inorganic perovskites in various kinds of applications, including lighting and visible light communication (Chap. 3), laser (Chap. 4), solar cells (Chap. 5), photodetectors (Chap. 6), high-energy radiation detectors (Chap. 7), as well as electronic devices (Chap. 8), have been described and discussed. In addition, strategies and mechanisms to improve their performance are presented. Finally, current challenges and overall outlook of inorganic perovskite applications are provided in order to promote the fundamental understanding and commercial development in various directions.

We express our gratitude to our colleagues, including Baiqian Wang, Ruoyu Peng, Xiaochen Wu, Yu Zheng, Ming Yang and Zhichen Wu at Chongqing University for their assistance in organizing the seminar and editing this book. We also extend our

appreciation to the editors of Springer Nature for inviting us to write this book, and we are delighted to have the opportunity to publish this book on inorganic perovskites.

Chongqing, China   Zhigang Zang
                                                                                                Shuangyi Zhao
                                                                                                     Wensi Cai
                                                                                                 Huaxin Wang

Contents

Chapter 1
Properties of Inorganic Perovskites

Abstract Inorganic metal halide perovskites (IMHPs) have emerged as a class of highly promising and cost-effective semiconductor materials for next-generation optoelectronic applications due to their remarkable properties, such as strong optical absorption, high luminescent efficiencies, long carrier diffusion lengths, and tunable bandgaps. The incorporation of various metal cations in IMHPs allows for their chemical components and structures to be regulated, leading to controllable modulation of their optoelectronic properties. In this chapter, we present a comprehensive introduction to the chemical components and crystal structures of IMHPs, including both classic inorganic lead halide perovskites and novel lead-free metal halides with perovskite and perovskite-like structures. Moreover, we provide a detailed summary of the optoelectronic properties and stabilities of IMHPs and how they change with the chemical components, crystal structure, size, temperature, and pressure. Additionally, we illustrate the novel self-trapped exciton mechanism of luminescence in lead-free metal halides and discuss their differences from classic lead halide perovskites.

1.1 Introduction

The rapid growth of modern industries has led to increased consumption of natural resources and energy, with lighting and displays alone consuming more than 20% of global electric energy annually [1]. The overuse of conventional fossil fuels and release of greenhouse gases have caused severe pollution and greenhouse effects. Thus, there is an urgent need to explore next-generation optoelectronic materials and develop technologies that conserve massive energy and reduce carbon release in the earth.

Metal halide perovskites, with the classic constitutional formula of ABX_3, where A and B represent organic/inorganic cations and metal ions, respectively, and X is the halide anions (Cl^-, Br^-, I^-), have attracted significant attention of researchers due to their excellent optoelectronic properties. Since 2009, when an organic metal halide perovskite semiconductor was first used as an absorption layer in efficient solar cells

[2], the rapid progress in metal halide perovskites has inspired more researchers to utilize them in lighting, visible light communication, lasers, solar cells, photodetectors, high-energy radiation detection, and electronic devices [3–9]. Despite the development of organic metal halide perovskites, their instability against water, humidity and heat impede further applications. Compared with organic perovskites, inorganic metal halide perovskite (IMHP) semiconductors with inorganic A ions of alkali cations are found to possess enhanced stability and excellent optoelectronic performance, making them one of the potential semiconductors [10, 11].

This chapter introduces the basic details of IMHPs, including their chemical components and crystal structures, and presents octahedral and tolerance factors used to evaluate stability of IMHP semiconductors. Besides, novel lead-free metal halides with perovskite and perovskite-like configurations are reviewed. Furthermore, the optoelectronic properties, such as strong optical absorption, high luminescent efficiencies, and long carrier diffusion lengths, as well as excellent stabilities of IMHPs are discussed. The appearance of structural changes and phase transitions of IMHPs due to the variety of chemical components, crystal structure, sizes, temperatures, and pressures result in changes in optoelectronic properties. The variations in optoelectronic properties with these factors are presented, and distinguished luminescent performance originating from a novel self-trapped excitons mechanism is illustrated. Finally, strategies to enhance stabilities of IMHPs are summarized and analyzed.

1.2 Chemical Components and Crystal Structures in IMHPs

1.2.1 Chemical Components and Crystal Structures in IMHPs

The basic chemical formula of classic IMHPs is ABX_3, in which the A and B represent alkali ions, such as Cs^+, K^+, Rb^+ and Na^+, and divalent metal cations (Pb^{2+}, Sn^{2+}, Zn^{2+}, Eu^{2+}, Mn^{2+} etc.), respectively [12, 13]. The X is the halide anions (Cl^-, Br^-, I^-). As a typical ABX_3-type IMHP, $CsPbBr_3$ exhibits a cubic phase and three-dimensional (3D) configuration [14]. As shown in Fig. 1.1, the "Pb^{2+}" cation is surrounded by six nearest-neighbor "Br^-" anions, while the "Cs^+" cation sits in a cavity formed by eight corner-sharing $[PbBr_6]$ octahedral [15]. Besides, with an increase in amounts of CsBr containing Cs^+ and Br^- ions, it has been observed that $CsPbBr_3$ can transform to a trigonal Cs_4PbBr_6 with a zero-dimensional (0D) structure resulting from the isolation of $[PbBr_6]$ octahedra by Cs^+ cations [16]. Removal of CsBr or addition of $PbBr_2$ to Cs_4PbBr_6 can restore $CsPbBr_3$. Additionally, $CsPb_2Br_5$ can be obtained by incorporating a small amount of $PbBr_2$ into $CsPbBr_3$, which features a two-dimensional (2D) layered $[PbBr_6]$ configuration isolated by Cs^+ ions. Apart from stoichiometric numbers, the incorporation of organic ligands and solvents can also lead to the phase transformation of cubic $CsPbBr_3$ to an orthorhombic structure,

Fig. 1.1 Structural models of **a** 3D cubic $CsPbX_3$ and **b** 0D hexagonal Cs_4PbX_6 perovskites with X = Cl, Br, I [15]. Copyright 2017, American Chemical Society
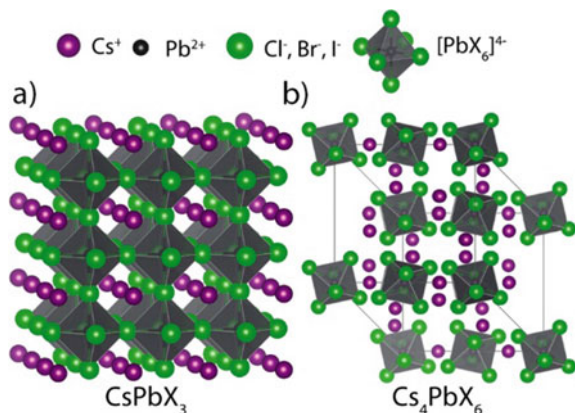
where a distorted 3D configuration is attributed to Cs^+ vacancies in its crystal network. It is noteworthy that incorporation of inorganic ions and organic groups can cause changes in crystal configuration and dimensions, as well as phase transformation of inorganic lead halide perovskites.

$$Cs_4PbBr_6 \overset{\pm CsBr}{\leftrightarrow} CsPbBr_3 \overset{\pm PbBr_2}{\leftrightarrow} CsPb_2Br_5$$

Additionally, the impact of different halide anions on crystal lattices of $CsPbX_3$ has been extensively studied. The lattice constant of the perovskites is found to gradually decrease as the ionic radius of halide anions decreases ($R_I > R_{Br} > R_{Cl}$), resulting in a reduction in lattice constant from 6.20 Å ($CsPbI_3$) [17] to 5.60 Å ($CsPbCl_3$) [18]. Moreover, the crystal structure of inorganic perovskites can continuously change due to variations in temperature and pressure, leading to deformation of bond angles and bond lengths between B-site metal and X-site halogen ions. While the temperature and pressure may cause the distortion of $[BX_6]$ octahedra, the 3D configuration of $CsPbX_3$ remains unchanged, with bond angles ranging from 180° to 150°. $CsPbBr_3$ exhibits α-β and β-γ phase transitions at 130 °C and 88 °C, respectively [19, 20]. Similarly, with an increase in temperature, $CsPbI_3$ undergoes a noticeable phase transition from β- to α- phase at 184 °C and 281 °C, respectively. At room temperature, yellowish $CsPbI_3$ exists as the δ-phase.

1.2.2 Chemical Components and Crystal Structures in IMHPs with Single Lead-Free Ions

In addition to inorganic lead halide perovskites, lead-free metal halides have been synthesized by substituting Pb^{2+} with other metal ions, including monovalent (Cu^+), divalent (Sn^{2+}, Zn^{2+}, Zr^{2+}, Mn^{2+}), trivalent (Bi^{3+}, Sb^{3+}, In^{3+}), and tetravalent (Sn^{4+},

Pd^{4+}) elements. It has been observed that the presence of monovalent, tri- and tetrava-
lent cations results in formation of various structures and configurations with typical
3D ABX$_3$ perovskites. As shown in Fig. 1.2a, metal halides with B^{3+} and B^{4+}
cations exhibit chemical formulas of A$_3$B$^{3+}_2$X$_9$ and A$_2$B^{4+}X$_6$, respectively, while a
combination of a monovalent and trivalent cation can form A$_2$B$^+$B^{3+}X$_6$ type double
perovskites [21].

As mentioned earlier, the metal halide polyhedra are considered as the primary
building blocks of perovskites, and they play a crucial role in determining the struc-
tural stability of these compounds. Therefore, replacing Pb^{2+} with lead-free metal
cations is expected to cause deformation, disorder, and even destruction of metal
halide polyhedra due to differences in size among metal cations and halides. To eval-
uate the structural stability of metal halide polyhedra, an octahedral factor (μ) has
been proposed, which is the ratio of ionic radii of B-metal and halide:

$$\mu = \frac{r_B}{r_X} \tag{1.1}$$

where the r_B and r_x are the ionic radii of lead-free metal cations and halide anions,
respectively, and the ideal range of μ for a stable octahedron is 0.377–0.895 [22].
Apart from metal halide polyhedra, the A-site cations are important because it can
determine the symmetry of structures and stability of phases. The Goldschmidt's
tolerance factor (t), which depends on the ionic radius of the lead-free ions and is an
empirical parameter, is introduced to evaluate the symmetrical structure as following:

$$t = \frac{(r_A + r_B)}{\sqrt{2}(r_B + r_X)} \tag{1.2}$$

The idea range of t for perovskites is 0.813–1.107, and a 3D symmetric struc-
ture can form when t close to 1 [23]. Experimental findings indicate that the three-
dimensional crystal structure of IMHPs exhibits excellent physical and chemical

Fig. 1.2 **a** Schematic relation between the crystal structures of Pb-based perovskites and lead-free
perovskite derivatives [21]. Copyright 2016, American Chemical Society. **b** Map of (t, μ) for 138
perovskite compounds considered. Red dots mean ΔHD > 0 (predicted to be stable), and black dots
mean ΔHD < 0 (predicted to be unstable) [24]. Copyright 2017, American Chemical Society

properties when the t are in the range of $0.81 < t < 1.11$, making them highly applicable in solar cells, sensors, and other fields. However, when $t < 0.89$, octahedral units of perovskites could distort, leading to a low symmetric quadrantile phase (β phase, P4/mbm space group) and a tetragonal phase (γ phase, Pbnm space group). Similarly, highly distorted structures are observed when $t > 1$. Further increase of t above 1.13 produces layered structures with face-sharing octahedra. If the calculated t value of a certain perovskite falls outside the range, the original structure of the perovskite may convert to an asymmetric one, resulting in a transformation from a cubic phase to a tetragonal or orthorhombic phase. In case the t value of a perovskite significantly deviates from 1, its three-dimensional structure may undergo torture, warping, and destruction, leading to a low-dimensional structure (0D, 1D, and 2D). Consequently, these low-dimensional perovskites possess wide band gaps and large exciton binding energy, which make them unsuitable for single perovskite solar cells. Nevertheless, these materials exhibit potential as light-absorbing materials in series solar cell structures as well as significant applications in ion conduction and ferroelectricity.

Yin et al. proposed a new factor of $(t + \mu)^\eta$, in which the η represents the atomic packing fraction which is defined as the fraction of volume in a crystal structure that is occupied by neighed atoms [24]. By calculating 138 inorganic metal halides (Fig. 1.2b), a linear relationship between decomposition energies (ΔHD) and ($t + \mu)^\eta$ is found, in which the prior value can be utilized to evaluate thermodynamic stabilities of IMHP semiconductors. With the assistance of t, μ and $(t + \mu)^\eta$, structural stabilities of novel lead-free metal halide perovskites can be predicted successfully, which have been beneficial in exploration and preparation of lead-free metal halide perovskites with different B-site metal ions.

According to calculating results, monovalent copper (Cu^+) ion has been identified as a promising alternative to lead in inorganic metal halide perovskites. However, due to the high energy level and instability of its $3d^{10}$ orbitals, the Cu^+ ion may undergo hybridization of 4 s and 4p orbitals to reduce the energy. Moreover, the Cu^+ ion has a small ionic radius of 0.60 Å, resulting in its coordination with only three or four halide ions to form a stable Cu^+-X^- polyhedron compared to the Pb^{2+} ion. This leads to the preference of Cu^+ ion to form a $[CuX_3]$ trigonal or $[CuX_4]$ tetrahedral coordination with halide ions. In 2018, Hosono et al. reported the synthesis of $Cs_3Cu_2I_5$ single crystal, which exhibited an orthorhombic configuration with a Pnma space group [25]. In the $Cs_3Cu_2I_5$, its basic unit of a $[Cu_2I_5]^{3-}$ dimer consists of an edge-sharing $[CuI_3]$ trigonal and a $[CuI_4]$ tetrahedron, which are isolated by the inorganic Cs^+ cations. As shown in Fig. 1.3, the crystal structure of $Cs_3Cu_2I_5$ is 0D configuration, but the reported $CsCu_2X_3$ (X = Cl, Br, I) exhibits 1D orthorhombic configuration, where the $[CuI_4]$ tetrahedra are edge-sharing contacted with each other to form several 1D $[Cs_2I_3]_n$ chains [26, 27]. In contrast, other A_2CuX_3-type materials, such as Rb_2CuX_3 and K_2CuX_3, are configured with stacking corner-sharing $[CuI_4]$ tetrahedra along their 1D direction [28–30].

Due to their similar valence to Pb^{2+}, bivalent lead-free ions are promising alternatives in inorganic lead-free metal halide perovskites, as they exhibit similar crystal structure and phase. Among these, Sn^{2+} is of particular interest due to its electronic

Cs$_3$Cu$_2$X$_5$

CsCu$_2$X$_3$
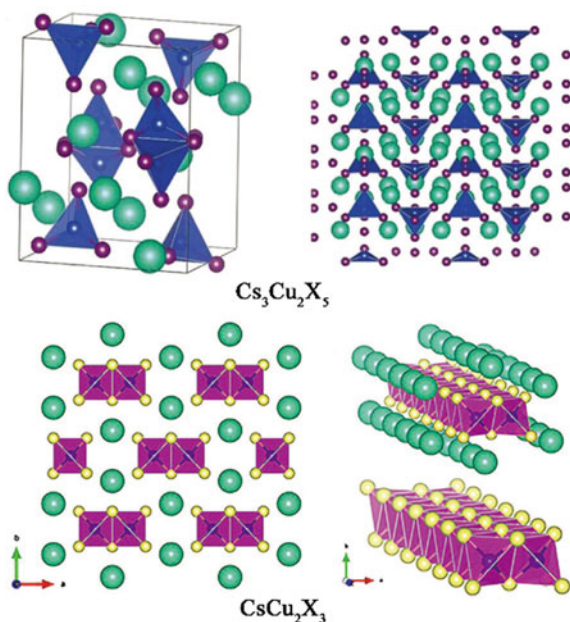
structure and ionic radii being comparable to those of Pb^{2+}. It is expected that Sn^{2+} would form a 3D structure with ideal cubic symmetry. However, the plasticity of Sn-X bonds may cause the deformation of Sn-X octahedra, leading to a phase transition from cubic to tetragonal at room temperature. Additionally, the oxidation of Sn^{2+} to Sn^{4+} can result in the distortion of cubic structures, leading to the phase transition. Kanatzidis et al. observed a phase transition in CsSnI$_3$ from a black cubic (B-α) to a black tetragonal phase (B-β) at 426 K, followed by a black orthorhombic phase (B-γ) at 351 K [31]. Finally, the B-γ phase transformed into a yellow polycrystalline phase after exposure to air for 1 h, as shown in Fig. 1.4 [31]. Here, the B-α, B-β, B-γ, and Y phases correspond to cubic, tetragonal, orthorhombic, and orthorhombic structures, respectively. Apart from Sn^{2+}, other bivalent ions such as Ca^{2+}, Sr^{2+}, Mn^{2+}, Zn^{2+}, Cu^{2+}, and Eu^{2+} can also be used to synthesize metal halides with various configurations, such as cubic, tetragonal, and orthorhombic. However, not all bivalent lead-free ions form regular metal-halide octahedra. For example, in CsMnCl$_3$(H$_2$O)$_2$ metal halides, a Mn^{2+} ion is surrounded by two O^{2-} and four Cl$^-$ ions, forming a distorted [MnCl$_4$(H$_2$O)$_2$] octahedron [32]. As the [MnCl$_4$(H$_2$O)$_2$] octahedra are connected along a (100) direction and separated by Cs$^+$ ions, the final dimension and crystal structure of CsMnCl$_3$(H$_2$O)$_2$ are 1D and orthorhombic, respectively [33]. Additionally, CsCuCl$_3$ exhibits a unique DNA-like double helix configuration due to the connection of Cu-Cl tetrahedra in the z-direction, which distinguishes it from other ABX$_3$ perovskites.

Trivalent metal ions, specifically IIIA and VA cations neighboring Pb, have been explored as promising alternatives for inorganic lead-free perovskites with a formula
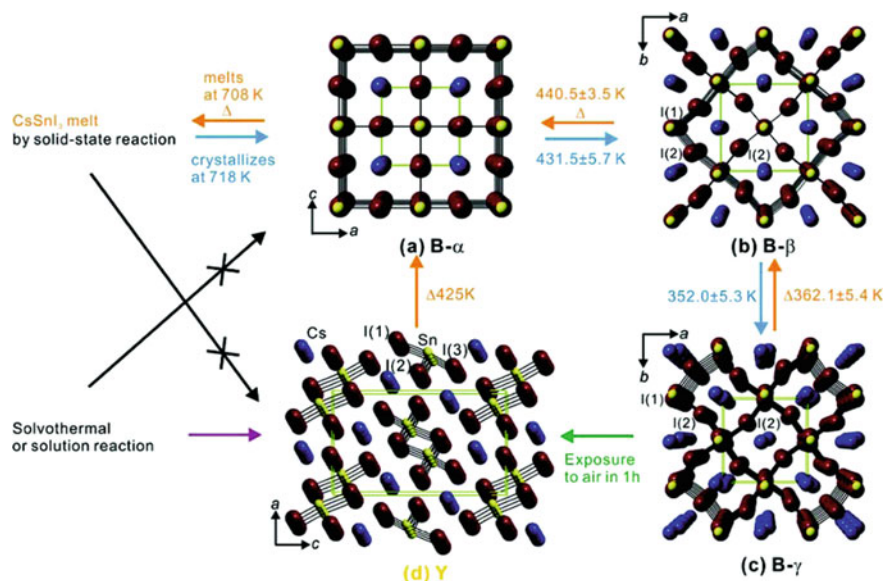
Fig. 1.4 Illustration of phase transformation details of four $CsSnI_3$ crystals and their crystal structures. The blue, dark red, and yellow balls correspond to Cs^+, I^-, and Sn^{2+} ions, respectively. Reproduced with permission [31]. Copyright 2012, American Chemical Society

of $A_3B_2X_9$. Among bivalent metal halides, Bi^{3+}-based compounds have been synthesized and investigated due to their enhanced stabilities and suitability for solution-based synthesis. Despite the presence of Bi-X octahedra in all $A_3Bi_2X_9$ families, two distinct crystal structures have been identified with cubic and hexagonal close packing of A and X ions, respectively. Among them, $Cs_3Bi_2I_9$ exhibits a $[Bi_2X_9]$ unit resulting from face-sharing $[BiX_6]$ octahedra in a 0D configuration, while $K_3Bi_2I_9$ and $Rb_3Bi_2I_9$ tend to form layer-like 2D structures with the assistance of vacancies ($\square$) [35]. In these 2D structures, Bi^{3+} ions occupy only two-thirds of the $[BiX_6]$ octahedral spaces, resulting in a cubic configuration of $Rb(Bi_{2/3}\square_{1/3})I_3$ and $K(Bi_{2/3}\square_{1/3})I_3$ [34]. Another trivalent alternative to Pb is antimony (Sb) with a chemical formula of $A_3Sb_2X_9$, exhibiting a 2D configuration containing a basic unit of Sb_{3+}-X^-. The crystal configurations and dimensions of these $A_3Sb_2X_9$ and $A_3Bi_2X_9$ compounds are influenced by the combination of alkali cations and halide anions, which can act as fillers or separators between $[BX_6]$ octahedra layers. The resulting structures can be either 2D or 0D, depending on the size of the alkali ion. For instance, Cs^+ ions with larger ionic radii tend to "cut down" and split the original 2D structure to 0D, as illustrated in Fig. 1.5 [34]. Trimmel et al. observed that halide ions may increase the crystal lattice and cell volume of $Rb_3Sb_2Br_{9-x}I_x$, but not alter the original 2D monoclinic structure. Another trivalent ions, indium (In^{3+}), are also reported to form $A_3In_2X_9$-type perovskites. In addition to Sb and Bi, indium (In^{3+}) can also form $A_3In_2X_9$-type perovskites, as well as $AInX_5 \cdot H_2O$-type metal halides with 0D structures [36]. Due to the strong binding energy of In-O bonds, the $[InX_5O]$ octahedra
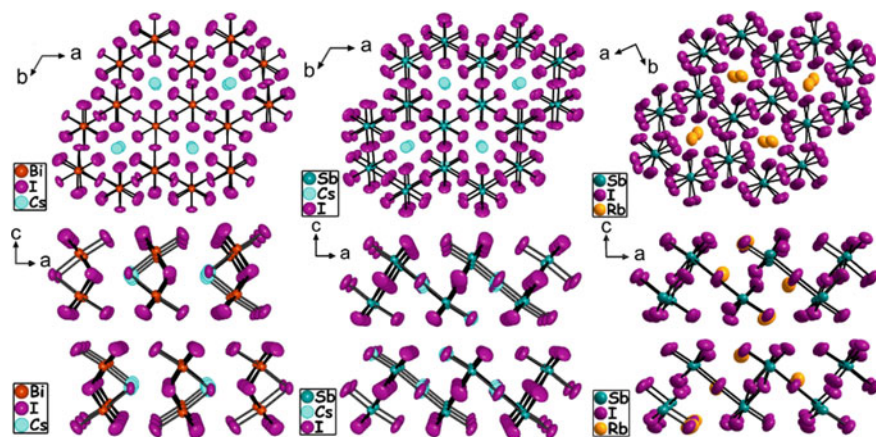
Fig. 1.5 Crystal structure comparison of $Cs_3Bi_2I_9$ (left), $Cs_3Sb_2I_9$ (middle), and $Rb_3Sb_2I_9$ (right) as viewed down the c-axis and along the b-axis, respectively [34]. Copyright 2017, American Chemical Society

are expected to be distorted and asymmetric, resulting in orthorhombic configuration and phase transformation under heating.

Metal halides with Sn^{4+}, Te^{4+}, and Pd^{4+} ions, represented by the general chemical formula of A_2BX_6, exhibit isolated B-X octahedra by A^+ cations and have 0D configurations [37–39]. With variations in A^+ and X^- ions, the lattice constants and cell volumes may change, but the A_2BX_6-type lead-free metal halides maintain their original cubic structures, indicating excellent chemical stabilities and high defect tolerance.

1.2.3   Chemical Components and Crystal Structures of Inorganic Double Perovskites

As discussed above, the majority of lead-free perovskites that are based on a single B-ion are unable to maintain their cubic crystal structures as observed in lead halide perovskites. Hence, significant emphasis has been placed on the investigation of inorganic lead-free metal halides that exhibit stable cubic structures and configurations similar to those observed in $CsPbX_3$ perovskites. Recently, a novel class of lead-free double perovskites containing two distinct metal cations has emerged and has demonstrated exceptional properties.

Inorganic lead-free double perovskites can be categorized into two main types: $A_2B^+B^{3+}X_6$-type and $A_4B^{2+}B^{3+}_2X_{12}$-type [40]. In the former type, two Pb^{2+} ions are replaced by a monovalent B^+ and a trivalent B^{3+} ion to ensure charge balance in $A_2B^+B^{3+}X_6$ double perovskites, as shown in Fig. 1.6 [13]. In $A_2B^+B^{3+}X_6$-type double perovskites, both B^+ and B^{3+} ions can occupy the centers of $[BX_6]$ octahedra
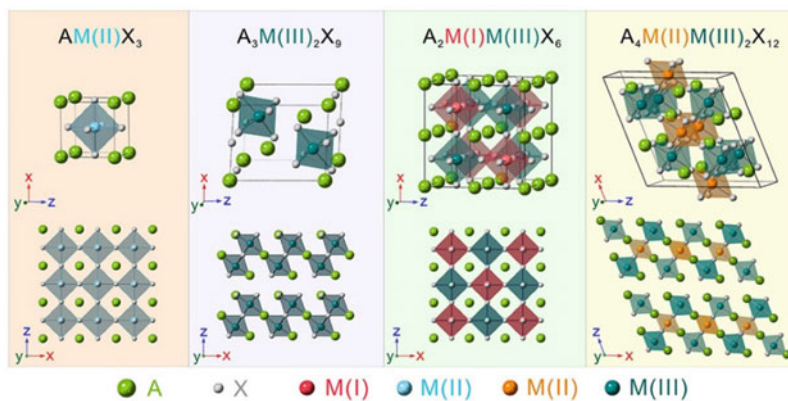
Fig. 1.6 Crystal structures of lead-free perovskites and double perovskites with different metal cations [40]. Copyright 2020, American Chemical Society

due to their proper ionic radii and ordinating numbers of six. Due to the intrinsic thermodynamic stabilities, a variety of $A_2B^+B^{3+}X_6$-type double perovskites, such as $Cs_2AgBiBr_6$, $Cs_2AgBiCl_6$, $Cs_2AgSbBr_6$ and $Cs_2AgSbCl_6$, have been prepared and reported [41–44].

For the latter type, three octahedron centers are occupied by a vacancy, a bivalent B^{2+} ion and a trivalent B^{3+} ion, respectively, where the layered double perovskite structure consists of one layer of $[B(II)X_6]^{4-}$ octahedra sandwiched by two layers of $[B(III)X_6]^{3-}$ octahedra in between two adjacent vacancy layers [45]. Although the $A_4B^{2+}B^{3+}{}_2X_{12}$-type double perovskites are found to be not close packing, their 2D structures exhibit thermodynamic stabilities. It has been reported that most $A_4B^{2+}B^{3+}{}_2X_{12}$-type double perovskites, such as $Cs_4CdSb_2Cl_{12}$ and $Cs_4CdBi_2Cl_{12}$, possess cubic crystal configurations [46]. However, owing to the lattice distortion induced by the existence of vacancies, $Cs_4MnBi_2Cl_{12}$ demonstrates a trigonal structure and sandwich layered configuration [47]. Its basic layered unit consists of corner-sharing $[BiCl_6]$-$[MnCl_6]$-$[BiCl_6]$ octahedra, which are broken by both Cs^+ cations and vacancies. Thus, compared with $A_2B^+B^{3+}X_6$-type double perovskites, $A_4B^{2+}B^{3+}{}_2X_{12}$-type double perovskites possess crystal feature and characteristic optoelectronic properties of low-dimensional semiconductors.

1.3 Properties of IMHPs

1.3.1 Electronic Properties

The unique electronic properties of inorganic perovskites arise from the distribution of energy states at the band edge and the dynamics of charge carriers. The electronic structure of IMHPs determines the distribution of energy states and types of bandgap. The distribution of the conduction band minimum (CBM) and the valence band maximum (VBM) in $CsPbX_3$ perovskites is determined by the Rashba effect and Dresselhaus splitting, and the band edge is composed of antibonding atomic orbitals of $[PbX_6]^{4-}$ octahedral [10]. As depicted in Fig. 1.7a, CBM is formed by the hybridization of 6p-orbitals of Pb^{2+} with s- and p-orbitals of X^- ions, whereas the VBM originates from 6 s- and 6p-orbitals of Pb^{2+} and s- and p-orbitals of X^- ions.

It should be pointed out that electronic states of the A-site cation do not directly influence the electronic structure of IMHP as they are far from the valence and conduction bands. Therefore, the major CBM and VBM in the electronic structure of inorganic lead-free metal halides are expected to arise from the orbits of lead-free metal cations (Bn^+) and halide anions (X^-). For example, in cubic $CsSnBr_3$ perovskites, the VBM and CBM are attributed to a mixture of 4p-orbitals of Br and 5 s-orbitals of Sn as well as 5p-orbitals of Sn, as illustrated in Fig. 1.7b [48]. Thus, electronic structures of IMHPs can be influenced by a variety of metal and halide ions, resulting in changes in bandgap types and values.

Although the direct devotions of ion orbits of A-site cations on electronic structures of IMHPs are negligible, the size of the A-site cations can cause lattice distortion of crystal structures and phase transitions in IMHPs. In addition, due to the strong correlation between their electronic structures and structural dimensionality, electronic structures of IMHPs are found to generally change as the decrease of their structural dimensionality. As shown in Fig. 1.8, $CsPbI_3$, Cs_2PbI_4, Cs_3PbI_5, and Cs_4PbI_6
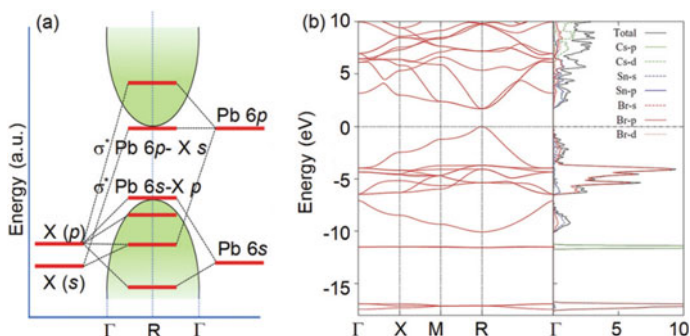

Fig. 1.7 a Band-edge states of halide perovskites [10]. Copyright 2016, American Chemical Society. **b** Band structure and partial density of states of $CsSnBr_3$ perovskites [48]. Copyright 2016, American Physical Society
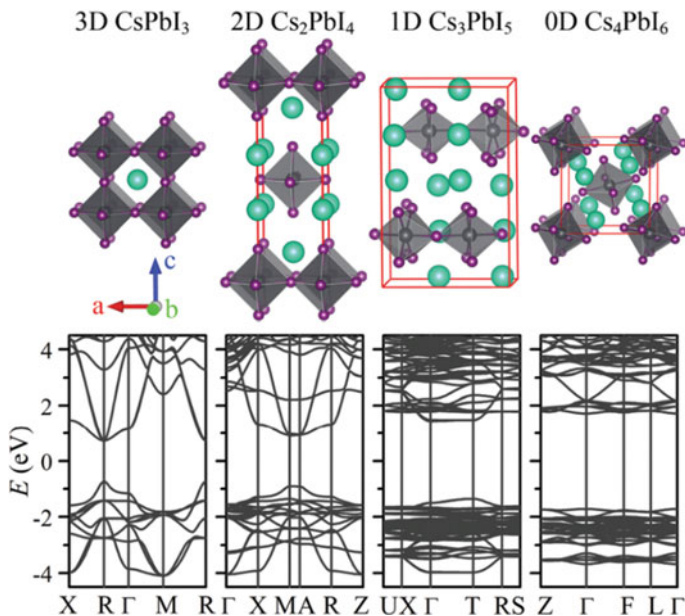
Fig. 1.8 Crystal structures and calculated band structures of $CsPbI_3$, Cs_2PbI_4, Cs_3PbI_5, and Cs_4PbI_6 [49]. Reproduced with permission. Copyright 2017, Royal Society of Chemistry

possess different structural dimensionalities, i.e., 3D, 2D, 1D, and 0D, respectively [49]. It is found that their bandgap increases with decreasing the electronic and structural dimensionality, showing 1.48, 1.90, 2.80, and 3.44 eV for the 3D, 2D, 1D, and 0D structures, respectively. As the structural dimensionality reduces from 3 to 2D, the band edges are relatively dispersive along the direction parallel to layers, but they are nearly flat along the direction perpendicular to layers, indicating that carriers are too heavy to move across layers. When further decreasing structural dimensionalities to 1D and 0D, bandgaps become too large and the band edges are localized, facilitating the enhancement of the exciton binding energy in low dimensional semiconductors.

Furthermore, the charge carrier dynamics is a fundamental electronic property in semiconductors. Among the electronic properties, the carrier diffusion process is of great importance because it can determine the diffusion length and carrier-carrier interaction [50]. The feature of carrier diffusion is characterized by the diffusion coefficient ($D_{n,p}$) and carrier mobility ($\mu_{n,p}$), which are related through the Einstein equation:

$$\mu_{n,p} = \frac{eD_{n,p}}{k_B T} \tag{1.3}$$

where k_B and e represent the Boltzmann constant and electronic charge, respectively. T is the temperature. And the diffusion length (L_D) of carriers is determined by their

$\mu_{n,p}$, and lifetime (τ) as the following equation:

$$L_D = \left(\frac{k_B T \mu_{n,p} \tau}{e}\right)^{\frac{1}{2}} = (D_{n,p}\tau)^{\frac{1}{2}} \qquad (1.4)$$

As depicted in the above equation, the prerequisite for long carrier diffusion lengths is high mobility and long carrier lifetime. The mitigation of traps is advantageous for enhancing carrier lifetime, while the lifetime can be affected by photon excitation, exciton recombination, and carrier transfer. When IMHPs are excited by photons with energy higher than the bandgap, charge carriers (electrons and holes) are generated in energy levels above the CBM with a non-equilibrium distribution in energy, commonly referred to as "hot carriers" [51]. These hot carriers engage in carrier-carrier scattering processes within 1 picosecond (ps) and subsequently may thermalize within the same timeframe. Thereafter, the hot carriers may undergo "cooling release" to the CBM or other band-edge states, achieving a quasi-equilibrium distribution [52].

Apart from photonexciton, the recombination and transfer of charge carriers within high energy states are other factors affecting the carrier lifetime [53]. The lifetime of carriers, which ranges from 10 ns to 100 ms, is determined by the electronic structures and types of IMHPs. In addition to these factors, the presence of traps and temperature can also affect the lifetime of carriers. Although radiative recombination is the only relaxation pathway for charge carriers in defect-tolerant perovskites, trap centers, which are caused by sub-bandgap energy levels arising from defects, can trap and detract carriers and lead to longer carrier lifetimes [54]. The effect of traps on the carrier dynamics can be studied using temperature-dependent photoluminescence characterization. For instance, the photoluminescence lifetimes of CsPbBr$_3$ decay become longer as the temperature increases, as shown in Fig. 1.9a, indicating the presence of defect states [55]. Moreover, CsPbBr$_3$ exhibits a low-energy photoluminescence peak at a low temperature of 70 K, which is attributed to the formation of localized trapped states between the bandgap (Fig. 1.9b, c) The detrapping process of CsPbBr$_3$ is suppressed at low temperature, leading to the formation of additional low-energy PL peaks, as shown in Fig. 1.9d.

In addition to the lifetime, the carrier mobility of IMHP is an important parameter of electronic properties. The carrier mobilities of IMHP films and single crystals are evaluated via a space-charge-limited current (SCLC) method. By depositing the metal electrodes on the IMHP films and single crystals to construct simple electrical devices. The current density versus driving voltages (J-V) curves of the IMHP are recorded and fitted with Mott-Gurney equation:

$$J_D = \frac{9\varepsilon\varepsilon_0\mu V_D^2}{8L^3} \qquad (1.5)$$

where J_D and V_D represent current density and driving voltage, respectively. ε is the relative dielectric constant, ε_0 is the vacuum permittivity, and L is the distance between two electrodes, μ can be calculated by fitting the Child region of J–V curves. The mobilities of IMHP are found to be affected by their trap density and surface
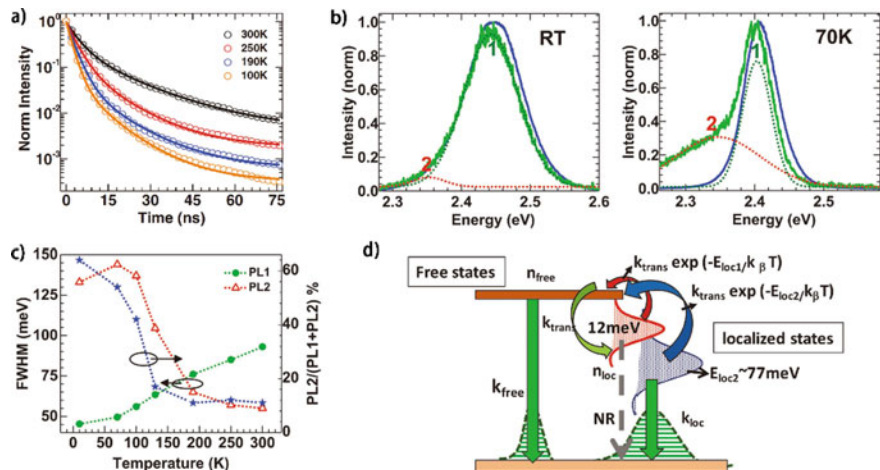
Fig. 1.9 **a** Temperature-dependent time-resolved integrated photoluminescence decay of $CsPbBr_3$ film for the temperature range T = 300 K to T = 100 K. Time-resolved photoluminescence spectra at **b** room temperature (RT) and **c** 70 K. **d** Schematic model of free versus localized exciton dynamics in $CsPbBr_3$ [55]. Copyright 2018, Wiley–VCH GmbH

morphologies. As a result, the improvement of crystalline quality and suppression of trap density facilitate to increase the carrier mobilities of IMHP films and single crystals. Figure 1.10a demonstrates the *J–V* curves of $Cs_3Bi_2I_9$ polycrystalline thin films (PCTF) and single-crystal thin films (SCTF), in which their mobilities can be fitted and calculated as 1.7×10^{-2} and 4.4×10^{-7} cm^2 V^{-1} s^{-1}, respectively [56]. The significant increased carrier mobility in single-crystal films than that in polycrystalline ones can be attributed in the reduction of traps density (n_t) in the grain boundary, which is calculated by the following equation:

$$V_D = \frac{en_t L^2}{2\varepsilon\varepsilon_0} \tag{1.6}$$

where the *e* is the electron charge. Compared with the high trap density in polycrystalline films (1.5×10^{15} cm^{-3}), single-crystal films exhibit a low trap density of 5.7×10^{12} cm^{-3}, clarifying the presence of higher carrier mobilities in single-crystal IHMPs. Besides, the optimized treatment in single-crystal IHMPs, such as incorporation of ligands and annealing, enables to enhance crystalline quality, resulting in the reduction of trap density. As shown in Fig. 1.10b, J-V curves of pristine and annealing $Cs_2AgBiBr_6$ single crystals were measured. By fitting results in Child areas, the pristine $Cs_2AgBiBr_6$ single crystal is found to possess a carrier mobility and trap density of 3.17 cm^2 V^{-1} s^{-1} and 5.4×10^9 cm^{-3}, respectively [57]. In contrast, the annealing single crystal showed high carrier mobility of 11.81 cm^2 V^{-1} s^{-1} and lower trap density of 1.74×10^9 cm^{-3}, confirming the important role of annealing treatment in the enhancement of electronic properties in IHMPs.
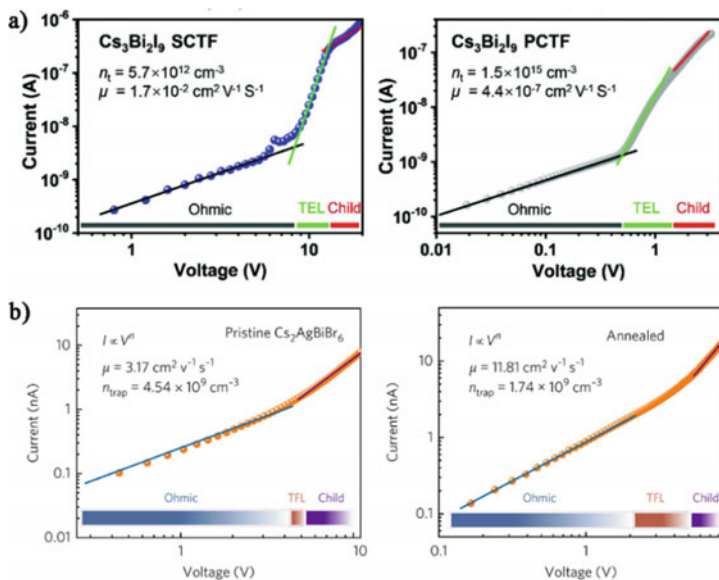
Fig. 1.10 a Current–voltage (*I–V*) characteristics of $Cs_3Bi_2I_9$ SCTF and PCTF using SCLC methods. Reproduced with permission. Copyright 2020, Wiley–VCH GmbH [56]. **b** *I–V* curves of pristine and annealed $Cs_2AgBiBr_6$ single crystals using SCLC methods. From the SCLC results, the trap density and carrier mobility are calculated and exhibited in the figures [57]. Reproduced with permission. Copyright 2017, Nature Publishing Group

Furthermore, electronic properties of IMHPs can also be significantly influenced by factors such as temperature, moisture, and high pressure. For instance, at low temperature such as 77 K, resistivity values of IMHPs tend to be higher due to the decrease in carrier concentration [58]. Similarly, in $Cs_2AgBiBr_6$, the resistance decreases with increasing moisture [59]. In another study, Zou et al. investigated the resistance changes of a $Cs_3Bi_2I_9$ single crystal under varying pressures [60]. The low-dimensional structure of $Cs_3Bi_2I_9$, which consists of isolated octahedrons, results in an initial resistance as high as 10^{11}–10^{12} Ω. However, as pressure is increased, the resistivity of the single crystal increases slightly and then drops dramatically to ~20 Ω at 28 GPa. Adding temperature to the equation, the resistivity of the single crystal was found to be ~110 Ω at 28 GPa at a temperature of 350 K. This increase in resistivity of low-dimensional IMHPs under high pressure and high temperature can be attributed to the reduction in distance among isolated octahedrons and the enhancement of orbital coupling caused by compression of the crystal structures.

1.3.2 Optical Properties

IMHPs have been known for their intriguing optical properties that are appealing for high-performance optoelectronic devices. The optical properties of these materials include strong and linear absorption, efficient and tunable photoluminescence throughout the visible spectrum, high-color purity, and high PLQY. In addition to these features, IMHPs exhibit optical performance resulting from a self-trapped excitons (STEs) mechanism. This includes broadband luminescence, long luminescent decay times, and large Stokes shifts in most low-dimensional lead-free metal halides.

Absorption

Optical absorption of IMHPs at a given frequency is regarded as a function of two primary parameters: the joint density of states (JDOS) and transition matrix from valance band states (VBS) to conduction band states (CBS). The Fermi's golden rule is used to approximate the relation between absorption performance and transition from VBS to CBS as following [61]:
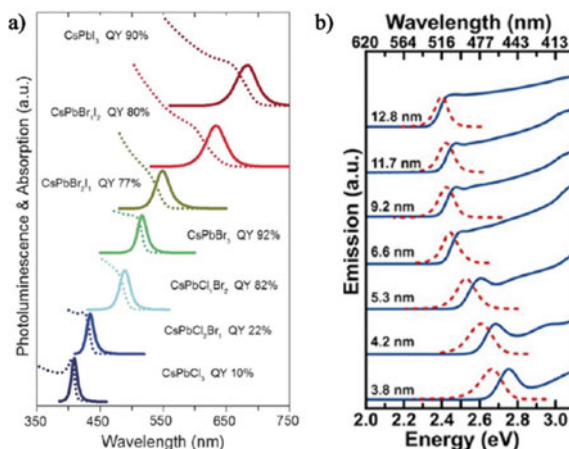
$$W_{\vec{k}} \cong \frac{2\pi}{\hbar} |v|\mathcal{H}|c|^2 \delta\left[E_c\left(\vec{k}\right) - E_v\left(\vec{k}\right) - \hbar\omega \right] \tag{1.7}$$

where the $E_c\left(\vec{k}\right)$ and $E_v\left(\vec{k}\right)$ represent the energy of CBS and VBS, respectively, and the $\mathcal{H}$ is the dipole operator. In most IMHPs, their intense optical absorption, which is found to originate from transition between halide p-orbits to metal p-orbits at the band edges [61, 62]. Due to the existence of p-orbits with less dispersion than s-orbits in IMHPs, their JDOS near the band edges shows is higher than other semiconductors, such as GaAs [63]. As a result, the optical absorption coefficients of IMHP are up to one order of magnitude higher than conventional semiconductors, such as GaAs and CuInSe$_2$ (CIS), in the visible range, indicating the strong absorption feature of IMHP semiconductors.

The optical absorption properties of IMHPs have garnered attention due to their potential use in high-performance optoelectronic devices. Several factors have been reported to influence the absorption spectra of IMHPs, such as chemical components, material size, temperature, and pressure. By changing the halide components (X) from Cl$^-$ to Br$^-$ to I$^-$, the absorption spectra of CsPbX$_3$ have been observed to broaden [64]. The optical absorption peaks of CsPbCl$_3$ and CsPbBr$_3$ nanocrystals were found to be located at ~415 and ~510 nm, respectively, while CsPbI$_3$ nanocrystals exhibited a strong absorption peak at ~645 nm, as shown in Fig. 1.11a. This shift in absorption peaks can be attributed to the change in the optical bandgap of materials.

Importantly, the size reduction of IMHP nanocrystals can lead to the quantum confinement effect, which affects their optical absorption performance. It has been reported that the quantum confinement effect of nanocrystals is size-dependent, the size ranges may be delimited: (1) if the sizes of nanocrystals are much larger than their exciton Bohr radius, the quantum confinement effect will be negligible; (2) When the sizes of nanocrystals are comparable with the exciton Bohr radius, the

weak quantum confinement effect may occur; (3) The strong quantum confinement effect can be observed when the sizes are smaller than the exciton Bohr radius, leading to the broadening of their bandgap induced by the shifts of CBM and VBM states [7]. As illustrated in Fig. 1.11b, the prepared CsPbBr$_3$ nanocrystals, with a size distribution ranging from 3.8 to 12.8 nm, demonstrate shifted absorption spectra due to the larger bandgap induced by the quantum confinement effect [65]. However, the varying range induced by the sizes is limited because of the confined changes of bandgap in IMHP nanocrystals.

Additionally, electronic structures of IMHPs can be varied by changing their metal components through doping and alloying, which can result in different crystal structures, phases, dimensions, and the incorporation of new energy levels. Due to the significant contribution of metal ion orbits in band edges, the absorption features of doped and alloyed IMHPs can differ from untreated ones. Figure 1.12a shows the absorption spectra of lead-free Cs$_2$AgIn$_x$Sb$_{1-x}$Cl$_6$ metal halides that have been alloyed, where Cs$_2$AgIn$_{0.5}$Sb$_{0.6}$Cl$_6$ and Cs$_2$AgSbCl$_6$ exhibit two distinct absorption edges, whereas others have only one [44]. These two edges correspond to the indirect absorption (smaller edge energy) and direct absorption with assisted photons (larger edge energy). By increasing the amount of Sb^{3+} ions, the transition of electronic structure types from direct to indirect in Cs$_2$AgIn$_x$Sb$_{1-x}$Cl$_6$ metal halides can be illustrated, as shown in Fig. 1.12b. The indirect Cs$_2$AgIn$_x$Sb$_{1-x}$Cl$_6$ metal halides with two absorption edges facilitate the expansion of the absorption range, which is crucial for practical applications in photovoltaics and photodetectors. Doping is another effective strategy to modulate the absorption performance of IMHP semiconductors.

Gao et al. doped Cu^{2+} ions into Cs$_2$AgBiBr$_6$ single crystals to broaden their absorption ranges [66]. Figure 1.12c illustrates the change in absorption spectra of Cu-doped Cs$_2$AgBiBr$_6$ with the increase of doped Cu^{2+} amounts. In comparison with intrinsic Cs$_2$AgBiBr$_6$ single crystals, which have a sharp absorption edge at 610 nm, the doped crystals show clear band tails in absorption spectra at 860 nm, mainly
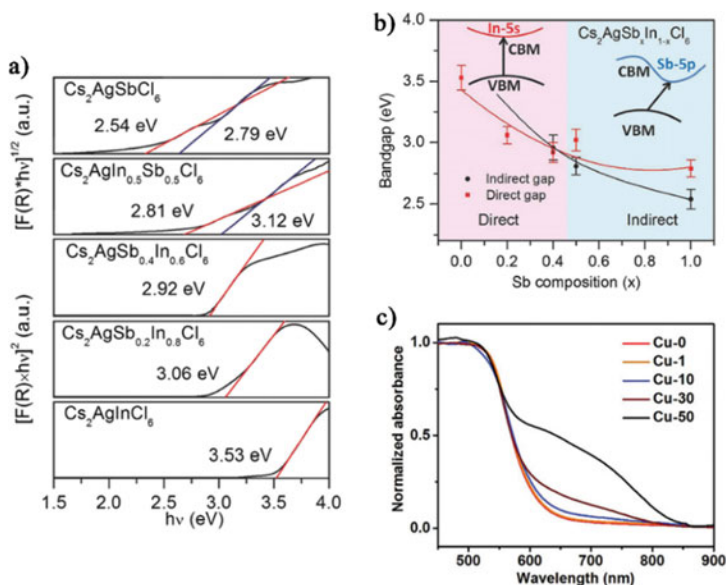
Fig. 1.12 **a** Tauc plots of absorption spectra of $Cs_2AgIn_xSb_{1-x}Cl_6$ metal halides. The transition of $Cs_2AgIn_xSb_{1-x}Cl_6$ bandgap from indirect to direct occurs at $x = 0.4$. **b** A schematic diagram of changes of bandgap for $Cs_2AgIn_xSb_{1-x}Cl_6$ metal halides [44]. Reproduced with permission. Copyright 2017, The Royal Society of Chemistry. **c** Absorption spectra of undoped and Cu-doped $Cs_2AgBiBr_6$ single crystals with various doped Cu^{2+} amounts [66]. Reproduced with permission. Copyright 2020, Wiley–VCH GmbH

due to the incorporation of a defect energy level induced by doped Cu^{2+} ions in the sub-bandgap of $Cs_2AgBiBr_6$ IMHPs.

The tunable absorption properties of IMHPs can also be modulated by applying pressure to the crystals. In a recent study, Zou and colleagues investigated the effect of pressure on the optical performance of a hexagonal $Cs_3Bi_2I_9$ single crystal using in-situ absorption characterization [60]. The results, as shown in Fig. 1.13, demonstrate that at atmospheric pressure, the $Cs_3Bi_2I_9$ single crystal exhibits an absorption edge at 603 nm. However, the band edge shifts to the near-infrared (NIR) range when the pressure reaches 13 GPa, resulting in a broadening of the absorption range. This phenomenon can be attributed to the narrowing of the bandgap induced by pressure. Interestingly, the indirect bandgap of $Cs_3Bi_2I_9$ single crystals was found to be maintained even under a high pressure of up to 16.5 GPa, indicating that pressure can be a promising strategy to broaden the absorption range of IMHPs without affecting the types of their electronic structures.

In addition to visible and NIR light, the X-ray can be absorbed by IMHPs. As shown in Fig. 1.14a, when absorbing incident X-ray photons, the electrons with variety of energy in the atoms of IMHP can interact with X-ray photons through several mechanisms, including the photoelectric effect, Rayleigh (coherent) scattering, Compton (incoherent) scattering, and pair production [67]. (1) Rayleigh
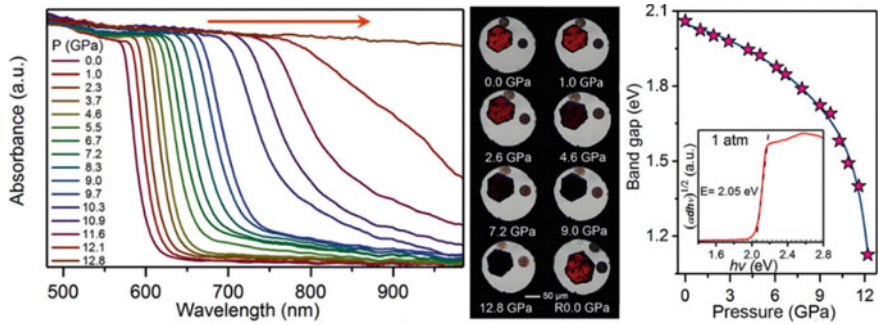
Fig. 1.13 Left: optical absorption spectra of a $Cs_3Bi_2I_9$ single crystal under high pressure. Middle: optical micrograph of a $Cs_3Bi_2I_9$ single crystal under high pressure. Right: band gap evolutions of $Cs_3Bi_2I_9$ under high pressure. The inset shows selected band gap Tauc plots for a $Cs_3Bi_2I_9$ single crystal at 1 atm. Reproduced with permission [60]. Reproduced with permission. Copyright 2018, Wiley–VCH GmbH

(coherent) scattering: X-ray photons are slightly scattered by the bound electrons with loss of negligible energy; (2) Compton scattering: photon changes its path and loses part of its energy to the recoil electron; (3) Photoelectric effect: the electrons absorb the whole energy of X-ray photon and then are ejected out from atoms; (4) Pair production: electron–positron pairs are found to produce when absorbing X-ray photons with high energy above 1.02 meV ($2m_ec^2$) [68]. The X-ray absorption ability can be evaluated by an absorption coefficient (μ) as the following equation:

$$\mu = \frac{\sigma_{\text{total}} N_A \rho}{Z} \tag{1.8}$$

where the σ_{total}, N_A and ρ represent total atomic cross section, atom concentration and mass density of the absorbers, respectively. Z is the atomic numbers of all elements
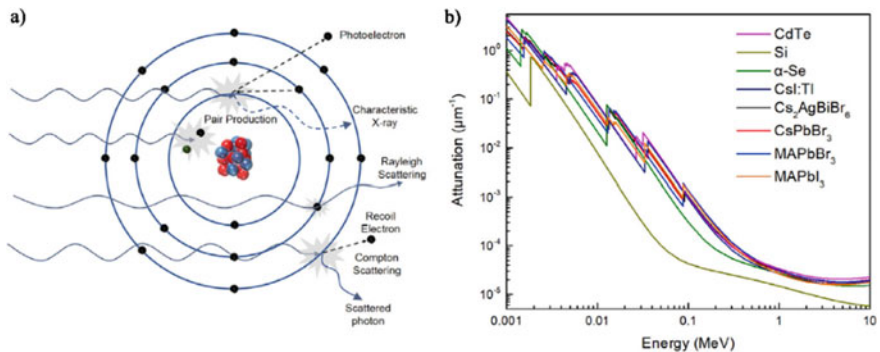

Fig. 1.14 a Basic features of photon interactions: photoelectric effect, Rayleigh scattering, compton scattering, and pair production. **b** The attenuation coefficients versus photon energy for some representative semiconductors [68]. Reproduced with permission. Copyright 2021, Cell Press